Optics Letters

Cavity-induced hybrid plasmon excitation for perfect infrared absorption

Alireza Safaei,[1,2] Sushrut Modak,[1,3] Abraham Vázquez-Guardado,[1,3] Daniel Franklin,[1,2] and Debashis Chanda[1,2,3,*]

[1]NanoScience Technology Center, University of Central Florida, Orlando, Florida 32826, USA
[2]Department of Physics, University of Central Florida, Orlando, Florida 32826, USA
[3]CREOL, The College of Optics and Photonics, University of Central Florida, Orlando, Florida 32826, USA
*Corresponding author: Debashis.Chanda@ucf.edu

Received 29 August 2018; revised 12 October 2018; accepted 17 October 2018; posted 17 October 2018 (Doc. ID 344258); published 11 December 2018

Photonic microcavity coupling of a subwavelength hole-disk array, a two-element metal/dielectric composite structure with enhanced extraordinary transmission, leads to 100% coupling of incident light to the cavity system and subsequent absorption. This light-funneling process arises from the temporal and spatial coupling of the broadband localized surface plasmon resonance on the coupled hole-disk array and the photonic modes of the optical cavity, which induces spectral narrowing of the perfect absorption of light. A simple nanoimprint lithography-based large-area fabrication process paves the path towards practical implementation of plasmonic cavity-based devices and sensors.

https://doi.org/10.1364/OL.43.006001

Subwavelength metal-dielectric resonators are excellent tools to enhance the light–matter interaction or control the phase of forward or backward scattering via local plasma oscillations [1,2] This is a direct result of the enhancement of the electric field at the surface plasmon resonance frequency which inherently depends on metal and dielectric optical properties and the geometry of the system [3,4]. Such a unique property offers a rich and broad gamut of applications, such as surface-enhanced Raman spectroscopy [5], biosensing [6], and flat optics [1,2]. Furthermore, these systems also allow fundamental physics study and understanding, such as cavity quantum electrodynamics [7,8], energy transfer [9], and superchiral light generation [10]. One of the disadvantages of surface plasmons is the inherent short lifetime resulting in a broad resonance spectrum due to the damped electron oscillations in the metals [11,12]. The coupling of plasmonic structures to the systems with narrow resonances is one route to reduce the resonance bandwidth which has been achieved by optical cavity coupling [5,13–15], free-space coupling [16,17], higher-order plasmon resonance coupling [18], and coupling to Fano resonances [19].

From these methods, photonic cavity resonant coupling has shown many interesting phenomena, such as amplified spontaneous emission [20], plasmon-cavity mode splitting [13,21,22], narrowband infrared radiation source [23], and efficient light trapping for solar cells [24,25]. All of these were based on the excitation of natural plasmon resonance and its coherent interaction with the cavity. Prior works theoretically showed perfect absorption in coupled metal/dielectric systems [26–28].

Here a cavity-assisted surface plasmon excitation on hole/disk array has been used to trap the incident photons which subsequently get absorbed as plasma loss. We show that the extraordinary transmission through the hole-disk system leads to the "funneling" of photons when coupled with an optical cavity. The cavity-induced and geometrically tunable funneling of photons through a subwavelength aperture [$\lambda \gg$ diameter(D)] leads to complete light absorption. This cavity-coupled hole-disk array behaves as a multi-resonance system in the other two wavelength regimes ($\lambda \sim$ D and $\lambda \ll$ D), as reported in our earlier works [5,13], which was based on the excitation of natural plasmon resonance in the visible spectral range (0.5–1.2 μm) and its coherent interaction with the cavity, the physics of which is completely different from that of this Letter. However, in the subwavelength regime ($\lambda \gg$ D), the complementary aperture pair, a hole and disk, when driven in-phase by the cavity to excite cavity-induced hybrid surface plasmons funnels ~100% of the incident photons through the subwavelength aperture. For a given disk and aperture dimensions, the peak absorption wavelength is tunable across a wide spectral range with the cavity phase.

There are two types of interaction between the optical cavity mode and the plasmonic mode. The first interaction type is related to the natural plasmonic modes of the hole-disk array which happens in the visible near-infrared wavelength regime where localized surface plasmon resonance (LSPR) depends solely on the geometrical parameters of the array. The coherent interaction of the plasmonic and cavity modes hybridizes the resonance mode and splits the absorption peak frequency [5,13,15,29]. Another interaction happens far from the natural LSPR, imposed by the fundamental cavity resonant mode which depends on the cavity phase [10]. Placing the disk array in the antinode locations of the cavity excites the surface plasmon via the spatial coupling between these two modes. Since the frequency of the trapped light excites the localized surface

plasmon on the disk array, the LSP mode is temporally coupled in-phase to the cavity mode. This strong coupling of the cavity and LSP mode and the very narrow bandwidth of the fundamental cavity resonance induce spectral narrowing of the perfect absorption of light.

At present, all cooled and uncooled mid-infrared (mid-IR) detectors being "bucket" detectors generate integrated spectral images in binary color formats (choices of any two pseudo colors) eliminating the spectral information. In addition, the narrowband infrared absorption spectroscopy has proven to be a very important tool in the detection and identification of airborne chemicals where pattern recognition is used as a post-processing step to compare the infrared spectrum of library molecules against the infrared spectra of airborne contaminants [30,31]. To date, very little research has been performed on frequency selective uncooled devices. In this context, the proposed narrowband absorber paves the path for frequency selective detection of infrared radiation. In order to demonstrate the feasibility, we designed and fabricated three spectrally de-tuned detectors and reported as a separate publication [32,33].

A 3D cartoon of the cavity-coupled hole-disk system is shown in Fig. 1(a). The square array of the hole-disk has a period P and diameter D, and the separation between the hole array and disk array is the relief depth (RD). The height of the cavity, measured from the surface of mirror at the bottom to the top hole array is C. The thickness of gold for the hole and disk arrays is kept constant at 30 nm and, for the back mirror, it is kept constant (200 nm). The cavity spacer dielectric has a refractive index of 1.56. The absorption spectrum of the tri-layer system is shown in Fig. 1(b) for the parameters P = 1.14 μm, D = 0.76 μm, RD = 280 nm, and C = 0.87 μm. A cross-sectional electric field in the structure at the resonance wavelength ($\lambda = 4.4$ μm) is shown in the inset of Fig. 1(b). The underlying mechanism of absorption can be understood by analyzing the resonant coupling between the constituents in the structure, namely the hole-disk coupling, disk-disk coupling and, moreover, the cavity and disk array coupling. The cavity-coupled disk array absorbs less than 10% of incident light, as shown in Fig. 1(b), which highlights the role of hole-disk coupling in the photon trapping.

The angular response of the absorber using a rigorous coupled wave analysis approach and experimental measurement shows that the perfect absorption up to $\theta_{inc} = 45°$ has less than a 20% change [32]. Since the surface plasmon on the disk array is excited by the fundamental cavity resonant mode, its spectral bandwidth depends on the FWHM of the optical cavity. A higher Q-factor of the cavity induces a narrower absorption bandwidth.

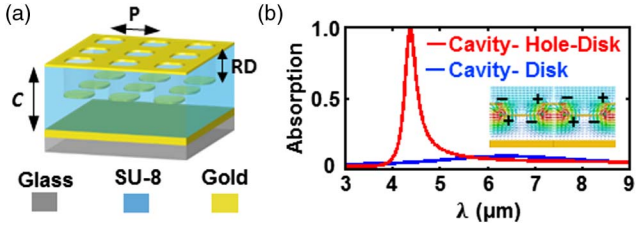

Fig. 1. (a) 3D schematics of the cavity-coupled hole-disk system. (b) Simulated (FDTD) light absorption in the cavity-coupled hole-disk array of period P = 1.14 μm, side D = 0.76 μm, C = 870 nm, and relief depth RD = 280 nm. Inset: computed electric field distribution inside the structure at resonance.

To show the role of the cavity in the narrowing of the bandwidth, we simulated the absorber system for different back-mirror thicknesses (0–20 nm). As shown in Figs. 2(a) and 2(b), with the decrease in the back-mirror thickness, the Q of the cavity reduces, resulting in both a higher FWHM and reflection.

Figure 2(c) shows the phase shift of the transmitted light imposed by the disk array from a finite-difference time-domain (FDTD) simulation. Most of the radiated energy from the disk in the upward direction is reflected back from the hole array, due to the subwavelength hole diameter, which acquires a phase shift of $\Delta\phi \approx \pi$ during reflection [13]. By passing through the disk array, the reflected field gathers another phase shift (ϕ_{disk}) such as in Fig. 2(c). This means that the reflected field acquires a total phase of $\phi_{ref} = 2\phi_{disk} + \pi$ which is in-phase with the downward radiation ($\phi_{trans} = \phi_{disk}$) over the spectral bandwidth $\lambda = 3$ μm – 5 μm, $\phi_{disk} \approx \pi$, resulting in constructive interference ($\phi_{ref} = \phi_{disk} + 2\pi$) and the transmission peak (blue), as seen in Fig. 3(a).

To understand the origin of the narrowband absorption in the cavity-coupled hole-disk array, first it is imperative to understand the mechanism of light funneling into the cavity through the cavity-uncoupled subwavelength hole-disk array. The light transmission of the unpatterned gold film (red), the hole array (green), the light transmission (blue), and the absorption (black) of the hole-disk array is shown in Fig. 3(a). While the light transmission of a 30 nm thick flat gold film is less than 1% and for the hole array is 7% at 3–9 μm, the hole-disk array has a transmission peak of 23% at 4.4 μm, and the absorption stays constant ~5% throughout the chosen wavelength range. It is well known that an array of subwavelength holes has an intrinsic extraordinary transmission of light compared to apertures of the same dimensions predicted by aperture theory and a larger than planar metal film of the same thickness, which is attributed to the excitation of surface plasmons on the edges of the holes and subsequent reradiation on the other side [34,35]. In the mid-IR spectral region, in the absence of natural plasmons, a perforated metal surface supports bounded surface waves or spoof plasmons to couple incident light to the metal and create localized charges around the holes [36,37]. In this coupled hole/disk system, these localized charges on the hole create complementary charge oscillations on the disk which can radiate light more efficiently compared to the hole. This is a direct result of the electric dipole moment of the disk array at resonance wavelength which is stronger than the hole array due to the higher charge concentration and longer lifetime of plasmons on the isolated disks (hence, a lower number of channels for radiation and resistive loss decay) [3,4,38].

The extraordinary transmission of the hole-disk array, when coupled to a photonic cavity, enables efficient coupling of

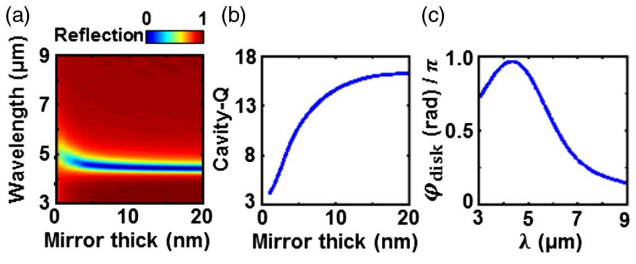

Fig. 2. (a) Reflection spectra as a function of wavelength and thickness of back-mirror. (b) Q-factor of the cavity-coupled absorber as a function of the back-mirror thickness. (c) Phase shift of the transmitted electric field through the disk array. (Mirror thick, the thickness of back-mirror.)

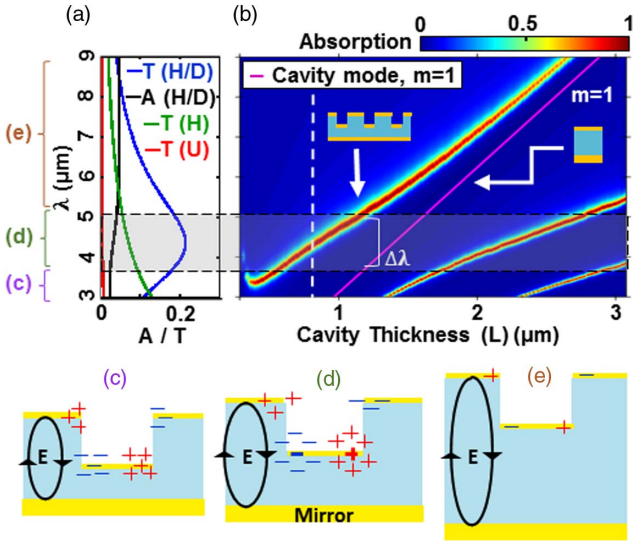

Fig. 3. (a) Light transmission of a 30 nm thick film without a pattern (red), with a subwavelength hole (green), and with coupled hole-disk (blue) arrays. The black diagram shows the absorption of a coupled hole-disk array. (b) FDTD predicted change in absorption as a function of the wavelength and cavity length of the system for the same system parameters as given in (a). The line cut (white dotted line) represents the plot in Fig. 1(b). (c)–(e) Cartoons depict the reason for the redshift of the resonant absorption peak as a function of the cavity height. Strength of the excited charges on the disk as a function of its depth in the cavity; the excitation is strongest at the antinode (shown in d) in the center of the optical cavity corresponding to the first cavity mode. (T, transmission; A, absorption; H, hole array; D, disk array; H/D, hole-disk array; U, unpatterned.)

light further. The simulated (FDTD) absorption spectrum as a function of the cavity length and wavelength is shown in Fig. 3(b) for parameters P = 1.140 μm, D = 0.760 μm, and RD = 280 nm. The predicted first-order ($m = 1$) Fabry–Perot cavity mode ($C = m\lambda/2n_{\text{eff}}$) corresponding to a simple planar cavity (magenta) has been plotted on top of the FDTD simulation. The presence of the disk array in the cavity not only adds an extra phase to the original cavity response, but also enhances the coupling of incident light even further. These roles of the hole array are explained in detail below. The deviation of the resonant absorption wavelength of the cavity-coupled hole-disk array from that of a simple cavity [Fig. 3(b) magenta plot] is due to the accrued extra phase shift in the presence of the disk array inside the cavity [1,14]. For the cavity resonance to exist, there must be an electric field antinode at $C_0/2$ or $\lambda/(4n_{\text{eff}})$ height in the cavity, where n_{eff} is the effective refractive index of the cavity spacer that in presence of surface plasmon sets the optical cavity length (C_0) shorter than the length of physical cavity (C). In this position, there is cavity-assisted surface plasmon excitation on the disk array [10]. For a constant RD, when the cavity length is increased, the disk array passes through the position of the enhanced electric field in the center of the cavity, introducing a large phase shift due to stronger electron plasma oscillations, and redshifts the total response. As the cavity height becomes much larger than the RD, this phase shift becomes comparatively low, and the response of the two systems asymptotically converges [in Fig. 3(b) for $C > 2$ μm]. This is pictorially represented in Figs. 3(c)–3(e). The light absorption of the cavity-coupled hole-disk array is near unity in the shaded region [Figs. 3(a)–3(b)], which corresponds to the resonance wavelength of the hole-disk array. As mentioned above, the presence of the disk array in the cavity redshifts the resonance by the excitation of charge oscillations on the surface. These oscillations are further enhanced when the position of the disk array is close to $C_0/2$ (antinode). This enhancement in the excited surface charges is coupled back to the upper hole array, strengthening the charge oscillations that are already present. This effect leads to the artificial enhancement of the light coupling into the cavity. The presence of the cavity also dictates a strict phase-matching condition for the complete absorption of light and, hence, the resulting bandwidth is very narrow ($\Delta\lambda/\lambda_{\text{res}} \sim 0.062$, FWHM = 270 nm at $\lambda_{\text{res}} = 4.4$ μm).

To understand the location of the losses in the cavity-coupled hole-disk array, full-vectorial simulation of Maxwell's equations is carried out. As shown in Figs. 4(a) and 4(b), due to the small lattice constant of disk array and edge-to-edge distance, charges on any disk element experience diagonal electric and adjacent magnetic forces. In addition, the charge oscillations on the disk also experience the charge oscillations on the hole due to strong hole-disk coupling as seen from the electric field distribution in the Fig. 1(b) inset. This combination of in-phase forces split the excited micro-currents on the disks to the edges. The simulated electric field, magnetic field, and current distribution on the surface of disk array are shown in Figs. 4(a), 4(b), and 4(c), respectively, for x-polarized light to prove our hypothesis. The surface plasma oscillations decay due to the resistive loss and hot-carrier generation due to Landau damping [4,11,12,39] which are responsible for the complete absorption of incident light. The coupled hole-disk array functions like a two-element optical antenna and induces extraordinary transmission through the sub-wavelength hole/disk array where the transmission efficiency depends on the coupling strength. The hole/disk coupling strength enhances further in the presence of the cavity inducing 100% coupling of the incident photons to the coupled system and zero back reflection. The edge current density on the hole-disk (**J**) array generates an Ohmic loss P = **J**·**E**, where **E** is the electric field, and P is the power loss. This power loss is responsible for the light absorption, as shown in Fig. 4(d).

Due to the plasmonic nature of the resonance, the resonant absorption wavelength scales as a function of the hole/disk size, as shown in Fig. 5. The proposed system is fabricated following a simple large-area nanoimprinting technique. A polydimethylsiloxane (PDMS) stamp is embossed against a photoresist (SU-8) layer spin-coated on a glass substrate coated with an optically thick (200 nm) gold mirror and followed by 2 h of UV exposure and 1 h of post-exposure bake ($T = 95$°C). This step forms

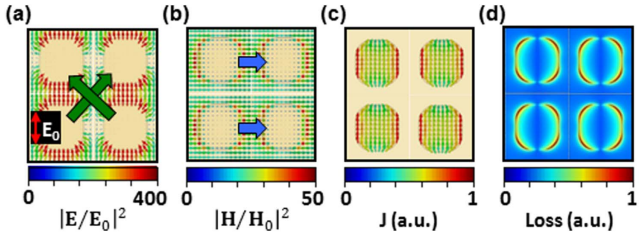

Fig. 4. Loss process in the cavity-coupled hole-disk system. FDTD predicted (a) electric field, (b) magnetic field, (c) current distribution, and (d) power loss distribution on the disk array.

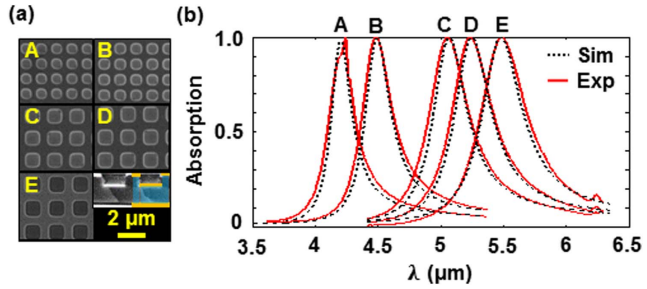

Fig. 5. (a) SEM images for five cavity-coupled absorbers with periods (P = 1.1, 1.14, 1.6, 1.66, and 1.74 μm in frames A–E) with a constant diameter-to-period ratio (D/P = 0.6). The inset shows the cross section of the quasi-3D structure. (b) Measured absorption spectra for the periods shown in part (a) along with simulated spectra for each pattern. (Sim, simulation; Exp, experiment.)

the hole array impression on SU-8 which further serves as the dielectric spacer ($C = 870$ nm) in the cavity. The blanket e-beam deposition of the thin layer (30 nm) of gold completes the simple fabrication process. The deposited gold forms the top perforated hole pattern on the raised region of the polymer imprint and the bottom disk array in the recessed region. Figure 5(a) shows the scanning electron microscope (SEM) images of five such representative systems with varied hole/disk diameters for constant D/P = (0.60 – 0.66). The corresponding optical photon capture via absorption measurements using a microscope-coupled Fourier-transform infrared spectroscopy (Hyperion 1000-Vertex 80, Bruker, Inc.), along with FDTD simulation predictions, appear in Fig. 5(b). As predicted, near 100% of the incident radiation is captured which is geometrically tunable.

In conclusion, this Letter demonstrates a unique cavity-phase-driven perfect absorption based on hybrid plasmon-induced extraordinary transmission through a subwavelength complementary aperture array producing a light funneling effect. The cavity-phase-driven and geometrically tunable photon capture and absorption, when coupled with a large-area nanoimprinting-based low-cost fabrication process, open up a new way of enhancing light–matter interactions for practical applications, such as frequency selective infrared detection, bio-sensing, and light harvesting.

Funding. Florida Space Grant Consortium (FSGC) (63019022); Northrop Grumman Mission Systems' University Research Program; Defense Advanced Research Projects Agency (DARPA) (HR0011-16-1-0003).

REFERENCES

1. A. Safaei, A. Vázquez-Guardado, D. Franklin, M. N. Leuenberger, and D. Chanda, Adv. Opt. Mater. **6**, 1800216 (2018).
2. N. Yu and F. Capasso, Nat. Mater. **13**, 139 (2014).
3. S. A. Maier, *Plasmonics: Fundamentals and Applications* (2007).
4. H. P. Paudel, A. Safaei, and M. N. Leuenberger, in *Nanoplasmonics—Fundamentals and Applications*, D. G. Barbillon, ed. (InTech, 2017).
5. D. Chanda, K. Shigeta, T. Truong, E. Lui, A. Mihi, M. Schulmerich, P. V. Braun, R. Bhargava, and J. A. Rogers, Nat. Commun. **2**, 479 (2011).
6. F. Yesilkoy, R. A. Terborg, J. Pello, A. A. Belushkin, Y. Jahani, V. Pruneri, and H. Altug, Light: Sci. Appl. **7**, 17152 (2018).
7. P. Ginzburg, Rev. Phys. **1**, 120 (2016).
8. F. Todisco, M. Esposito, S. Panaro, M. De Giorgi, L. Dominici, D. Ballarini, A. I. Fernandez-Dominguez, V. Tasco, M. Cuscuna, A. Passaseo, C. Ciraci, G. Gigli, and D. Sanvitto, ACS Nano **10**, 11360 (2016).
9. L. Y. Hsu, W. Ding, and G. C. Schatz, J. Phys. Chem. Lett. **8**, 2357 (2017).
10. A. Vazquez-Guardado and D. Chanda, Phys. Rev. Lett. **120**, 137601 (2018).
11. J. B. Khurgin, Nat. Nanotechnol. **10**, 2 (2015).
12. A. M. Brown, R. Sundararaman, P. Narang, W. A. Goddard III, and H. A. Atwater, ACS Nano **10**, 957 (2015).
13. A. Vazquez-Guardado, A. Safaei, S. Modak, D. Franklin, and D. Chanda, Phys. Rev. Lett. **113**, 263902 (2014).
14. R. Ameling and H. Giessen, Photonics Rev. **7**, 141 (2013).
15. A. Safaei, S. Chandra, A. Vázquez-Guardado, J. Calderon, D. Franklin, L. Tetard, L. Zhai, M. N. Leuenberger, and D. Chanda, Phys. Rev. B **96**, 165431 (2017).
16. L. Lin and Y. Zheng, Sci. Rep. **5**, 14788 (2015).
17. Z. Yong, S. Zhang, C. Gong, and S. He, Sci. Rep. **6**, 24063 (2016).
18. Z. Liao, Y. Luo, A. I. Fernandez-Dominguez, X. Shen, S. A. Maier, and T. J. Cui, Sci. Rep. **5**, 9590 (2015).
19. C. Yan, K.-Y. Yang, and O. J. F. Martin, Light: Sci. Appl. **6**, e17017 (2017).
20. G. Khitrova, H. M. Gibbs, F. Jahnke, M. Kira, and S. W. Koch, Rev. Modern Phys. **71**, 1591 (1999).
21. R. Ameling and H. Giessen, Nano Lett. **10**, 4394 (2010).
22. S. Chandra, D. Franklin, J. Cozart, A. Safaei, and D. Chanda, ACS Photonics (2018), doi: 10.1021/acsphotonics.8b00972.
23. Z. Wang, J. K. Clark, Y.-L. Ho, B. Vilquin, H. Daiguji, and J.-J. Delaunay, ACS Photonics **5**, 2446 (2018).
24. W. Wang, J. Zhang, X. Che, and G. Qin, Sci. Rep. **6**, 34219 (2016).
25. W. Ding and S. Y. Chou, in *IEEE 40th Photovoltaic Specialist Conference (PVSC)* (2014), pp. 2804–2807.
26. Y. Guo, L. Yan, W. Pan, B. Luo, and X. Luo, Plasmonics **9**, 951 (2014).
27. Q. Feng, M. Pu, C. Hu, and X. Luo, Opt. Lett. **37**, 2133 (2012).
28. M. Pu, C. Hu, M. Wang, C. Huang, Z. Zhao, C. Wang, Q. Feng, and X. Luo, Opt. Express **19**, 17413 (2011).
29. A. Safaei, S. Chandra, M. N. Leuenberger, and D. Chanda, "Wide angle dynamically tunable enhanced infrared absorption on large area nanopatterned graphene," 2018, http://adsabs.harvard.edu/abs/2018arXiv180600837S.
30. A. Dorodnyy, Y. Salamin, P. Ma, J. V. Plestina, N. Lassaline, D. Mikulik, P. Romero-Gomez, A. F. I. Morral, and J. Leuthold, IEEE J. Sel. Top. Quantum **24**, 1 (2018).
31. D. Chanda, A. Safaei, and M. N. Leuenberger, "Optical detector device with patterned graphene layer and related methods," U.S. patent 15,782,948 (April 19, 2018).
32. A. Safaei, S. Modak, J. Lee, S. Chandra, D. Franklin, A. Vasquez-Gaurdado, and D. Chanda, Opt. Express (to be published).
33. D. Chanda, S. Modak, J. Lee, and A. Safaei, "Optical frequency-selective absorber-based infrared detector, methods, and applications," U.S. patent 15,538,746 (February 15, 2018).
34. T. W. Ebbesen, H. J. Lezec, H. F. Ghaemi, T. Thio, and P. A. Wolff, Nature **391**, 667 (1998).
35. W. J. Fan, S. Zhang, B. Minhas, K. J. Malloy, and S. R. J. Brueck, Phys. Rev. Lett. **94**, 033902 (2005).
36. J. B. Pendry, L. Martin-Moreno, and F. J. Garcia-Vidal, Science **305**, 847 (2004).
37. R. Stanley, Nat. Photonics **6**, 409 (2012).
38. F. J. García de Abajo, Rev. Modern Phys. **79**, 1267 (2007).
39. R. Sundararaman, P. Narang, A. S. Jermyn, W. A. Goddard III, and H. A. Atwater, Nat. Commun. **5**, 5788 (2014).